Florida State University

SAE Aero Design East Competition

Team: 039

Team Captain: Alessandro Cuomo
Pilot: Tony Arnaoutis

Dimitrios Arnaoutis
Alessandro Cuomo
Eduardo Krupa
Gustavo Krupa
Jordan Taligoski
David Williams

Advisor: Dr. Chiang Shih

Tallahassee – FL
March 2012

Summary

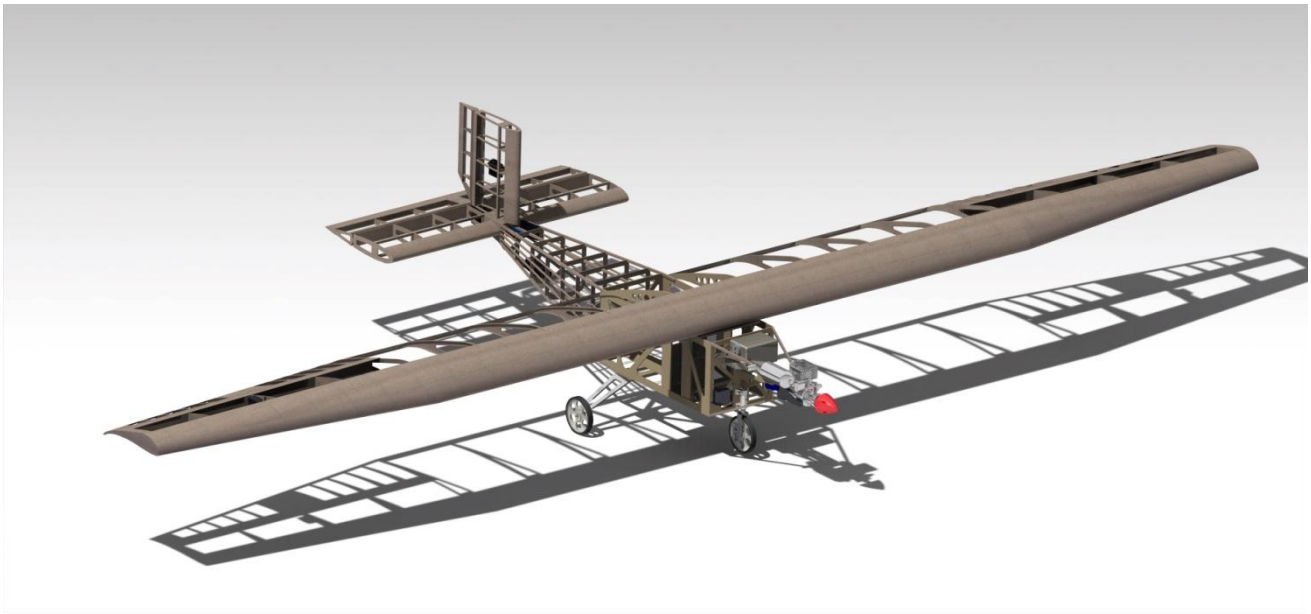

Statement of Compliance

Appendix
2012 SAE AERO DESIGN

STATEMENT OF COMPLIANCE

Certification of Qualification

Team Name	The Flying Spear	Team Number	039
School	Florida State University		
Faculty Advisor	Dr. Chiang Shih		
Faculty Advisor's Email	shih@eng.fsu.edu		

Statement of Compliance

As Faculty Advisor, I certify that the registered team members are enrolled in collegiate courses. This team has designed, constructed and/or modified the radio controlled airplane they will use for the SAE Aero Design 2012 competition, without direct assistance from professional engineers, R/C model experts or pilots, or related professionals.

Signature of Faculty Advisor

Team Captain Information:

Team Captain:	Alessandro Cuomo
Captain's E-mail:	ac08d@my.fsu.edu
Captain's Phone:	407-433-7010

Note: A copy of this statement needs to be included in your Design Report as page 2 (see 6.1).

Symbols List

h – Height

α –Angle of Attack

δ_{Trim} – Elevator Deflection Angle

δ_a – Aileron Deflection Angle

Λ – Sweep Angle

S – Surface Area

CG – Center of gravity

C_D – Aircraft Drag Coefficient

C_d – Profile Drag Coefficient

C_{D0} – Parasite Drag Coefficient

$C_{\mathcal{L}}$ – Lateral Stability Coefficient

C_h – Hinge moment Coefficient

C_m – Moment Coefficient

C_n – Directional Moment Coefficient

C_{m0} – Moment Profile Coefficient

η_v – Dynamic Pressure

C_L – Aircraft Lift Coefficient

C_l – Profile Lift Coefficient

C_V – Volume Coefficient

c – Chord

MAC – Mean Aerodynamic Chord

Δ – Deflection

ρ – Air density

D_L – Dimensional angular stability derivative of the rolling moment

N – Dimensional stability derivative

Y – Dimensional Lateral Stability Derivative

d – Distance

l_{CG} – CG distance – landing gear (x-direction)

h_{CG} – CG distance – landing gear(y direction)

X – Distance (x-axis)

η – Efficiency

b – Wingspan

ζ – Damping Factor

c_{at} – Friction Factor

e – Oswald's Factor

K – Pitch moment empirical factor

D – Drag Force

R – Reaction Force

L – Lift Force

ω – Frequency

l – Width

E – Modulus of Elasticity

M – Moment

I – Inertia Moment

W – Weight

P – Power

q – Dynamic Pressure

r – Radius

k – Radius of Gyration

A, AR – Aspect Ratio

A_1 – Inertia moment Ratio

η_{EH} – Relation between q_{EH}/q

Re – Reynolds

T – Thrust

V – Speed

μ – Air Viscosity

Vol – Volume

Index

a – Approach

a_l – Aileron

ψ – Slip Angle

β –Yaw angle

w – Wing

ac – Aerodynamic Center

c – Cruise

ds – Descend

d – Dynamic

dr – Dutch roll

s – Spiral

EH – Horizontal stabilizer

EV – Vertical stabilizer

fus – Fuselage

i – Induced

A – Maneuver

D – Dive

ml – Spring

p – Pitch

np –Neutral Point

B – Gust

G – Gear Ratio

rd – Wheel

g – Ground

td – Touchdown

tr – Transition

tp – Landing Gear

v – Vertical

r – Yaw

1. INTRODUCTION

The team "The Flying Spear" began the fall semester of 2011 as a collaboration between two universities: Universidade Federal de Itajubá [UNIFEI] and Florida State University [FSU]. The team consists of 4 FSU students two of whom traveled to UNIFEI in the fall to study and participate in the SAE Brazil competition and two UNIFEI students currently studying at FSU who have previously been involved with aero design teams to work together on an international design project whose objective is to design a lightweight, high payload capacity aircraft while observing the available power and aircraft's length, width, and height requirements as designated by the 2012 Regular Class requirements.

This report illustrates the preliminary design studies and the main aircraft characteristics. It consists of the calculations and decisions made throughout the conceptual, preliminary and detailed design processes. Sections 2 and 3 describe some of the considerations undertaken and details of the methodology implemented are outlined in Section 4. Section 5 describes the overall aerodynamic characteristics of the aircraft. Section 6 covers the stability and control analysis shown in order to validate the static and dynamic stability of the aircraft as well as the forces acting on the control surface. Section 7 contains the performance estimations and the final section describes the structural analysis conducted.

2. CONSIDERATIONS

The design point set to the aircraft was at steady flight while carrying maximum payload and at cruise speed. The following constants were used according to the standard condition for temperature and the pressure: $\rho = 1.2250$ [kg/m³] and $v = 1789 \cdot 10^{-6}$ [N.s/m²]. The value adopted for the acceleration of gravity was 9.8067 [m/s²]. The inertia moments were obtained from detailed drawings by means of the software CATIA®.

3. DESIGN

3.1.Methodology

The project methodology is based on seven steps: i) the gathering of information ii) preliminary studying iii) conceptual and preliminary studying iv) project development v) building of a prototype vi) ground testing vii) flight testing. The following design methodology is a compilation provided by Barros which originates from a synthesis of a methodology presented by Torenbeek (1981), Roskan (1985), Raymer (1989), Vandaele (1962), Stinton (1983), Wood (1968) and Frati (1946). This methodology presupposes a set of mission requirements; and based on these requirements the design itself will commence. Typical parameters include: payload and type of load, range, cruise speed and altitude, take-off and landing distance, fuel reserves, rate of climb requirements, maneuverability requirements, and certifications basis (i.e. will be adopted based on the FAR part 23 regulation rules as well as the competition's rules). The data will be collected and

estimated using a combination of the competition regulations and studies based on past designs. The team will couple this data using analytical equations that can be solved by means of an optimization tool. The results of said equations are to be plotted in a chart known as a "design chart"— extremely useful in determining the aircraft's design point. This will provide enough information to calculate the design lift coefficient, in which the preliminary design is heavily based. The next step is to perform the empty-weight estimation, takeoff-weight buildup, and fuel-fraction estimation. Having this data, it is possible to calculate the wind loads on the aircraft. Determining these parameters will allow us to estimate the wing load which is a vital variable to couple the aerodynamic/structural equations and thus the wing geometry and its respective aspect ratio and stall speed. The design philosophy will prioritize the L/D parameter; this most likely will be done by selecting airfoils with low drag and by fairing the aircraft. The drag estimation methods at the preliminary phase will be those taken from the series of books from ROSKAM. The next step is to choose a suitable airfoil; fortunately there is a vast online database featuring several airfoils from all types of aircrafts. The team will select the airfoil that best suits our criterion. If one is not found, the team will design one using inverse methods. At this point, wind tunnel testing will be conducted. The wing design methodology will start with analytical calculations, providing a first design point which will be modeled on the software Tornado VLM that runs on MATLAB. This software will be used to refine the wing planform and to calculate the most suitable twist and dihedral angle, in order to provide good stall characteristics and control. Having determined the wing geometry and its loads, it will be possible to complete the fuselage and tail-unit sizing. Computational tools were implemented in the stability and control derivatives evaluation, performance evaluation and cost estimation. If the results are satisfactory, the preliminary design phase will be complete.

3.2.Aircraft Characteristics

As a result of the above methodology, the main aircraft characteristics are summarized below:

Table 3.1 – Aircraft Characteristics

Aircraft			
Conventional monoplane aircraft			
Aircraft Empty Weight	3.00 [kg]	Engine	Magnum XLS-61A
Wheel Diameter	7.50 [cm]	Engine angle of incidence	0º
Distance between axes and landing gear	28.5[cm]	Propeller	11x7 *APC* Nylon Sport
Distance between the wheels of the main landing gear	40.0[cm]	Servo-Mechanisms	HXT-900,CS-35MG,CS12MG,CS-64MG,CS-12MG

Wing			
High tapered wing			
Root profile	Uirá 1540	Tip Profile	Uirá 1540
Chord profile	32.0 [cm]	Tip Chord	20.0 [cm]
Wing height measured from the ground	36.8 [cm]	Wing Area	1.45 [m²]
Wingspan	2.8 [m]	Aileron Area	696.25 [cm²]
Aspect Ratio	10.5	Dihedral Angle	7°
Horizontal Stabilizer			
Full-deflection, type "H"			
Profile	NACA 0016	Area	1319.99[cm²]
Chord	22.4 [cm]	Wingspan	60.0 [cm]
Vertical Stabilizer			
Duplo			
Profile	NACA 0016	Area	[cm²]
Chord	20.0 [cm]	Wingspan	60.0 [cm]
Materials utilized			
Balsa wood	Birch Plywood	Aluminum 6061	Nylon UHMW

4. AERODYNAMICS

The aerodynamic detailed design started with the geometry created as a result of the preliminary project. This allowed the team to define the requirements for the aerodynamic design. The literature utilized was BARROS [3] and RAYMER [1]. The team attempted to maximize the factor L/D since it affects the aircraft during all flight phases.

4.1 Profile Selection

The initial requirements were to design a profile that has at least $C_{L_{max}} = 2.08$. This value was calculated assuming that the aircraft could achieve its take-off speed (as seen in the performance section) with our maximum payload of approximately 165 N.

The associated Reynolds regime is in the order of 215,000. According to WHITE [4], the transition for a turbulent boundary layer occurs with a local Reynolds number, Re_x, that can be taken as $2.8 \cdot 10^5$, where x is the leading edge distance. The value of $Re_{x_{crit}}^{1/2}$ depends on the turbulence

intensity and is determined by the following semi-empirical relation where ζ is the turbulence intensity.

$$Re_{x_{crit}}^{1/2} = \frac{-1+(1+13{,}25\zeta^2)^{1/2}}{0{,}00392\zeta^2} \qquad (4.1)$$

Assuming a turbulence of ζ = 0.04 and plotting this result against the speed, the laminar flow was extended along 3% of the chord.

Table 4.1 – Profile Selection

Profile	$t/c(\%)$	$f(\%)$	$C_{l_{max}}$	$C_{d_{min}}$	C_m	C_l/C_d	Stall Type
Uirá1590	13.51	8.66	$2.33(alpha = 15°)$	0.0168736	−0.179	78.3	Smooth
Uirá1540	15.31	11.87	$2.64(alpha = 15°)$	0.0198286	−0.202	66	Abrupt

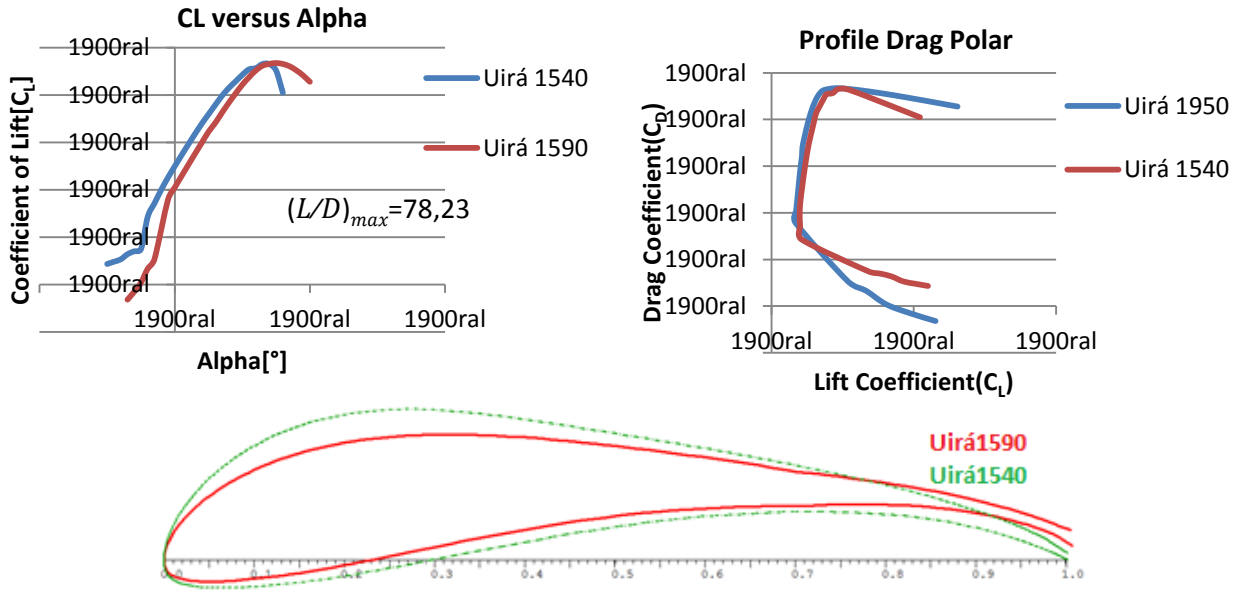

Figure 4.1 - Uirá 1540 and 1590 profile geometry

4.2 Wing

The wing design methodology consisted of systematic variations of the following geometric factors: wing area, taper ratio and taper location. For each iteration the following parameters were studied: Oswald efficiency factor, $C_{L_{max}}$, $C_{D_{min}}$ and C_m. The main advantages and disadvantages considered are summarized in the Table 4.2

Table 4.2 – Characteristics traded-off For the Wing and Empennage

Characteristics		*Advantages*	*Disadvantages*
Wing Location	*High Wing*	Low interference drag, high lateral stability, shorter landing (less ground effect)	Take-off is longer because of the reduction of the ground effect
Planform	*Recto-trapezoidal*	Combines the advantages of a rectangular and tapered wing in the sense that it exhibits reduced induced drag and has a smaller value for lateral inertia while being the most structurally sound option	The main disadvantage is the stall tendency in the aileron area
Empennage Type	*Conventional Tail*	Good response to the pitch command	Negative aerodynamic load in the horizontal empennage that may reduce the total lift
	T-tail	Only 2 points of aerodynamic interference, against 4 of the conventional tail	Building difficulties and deep stall risk

We selected the same profile from the wing root to the tip. The taper of the wing creates an area more susceptible to stall in the aileron; however, the stall must start at the beginning of the root to the tip and then over the ailerons in order to assure the lateral control of the aircraft even during the stall. For that we utilized the Armin Quast's orientation, found in BARROS [3], only after could we calculate a geometric twist of 2°.

4.3 Drag Polar

The drag polar was evaluated using a method proposed by BARROS [3] which takes in consideration the required elevator deflection to keep the aircraft in steady level flight. Also, it takes the length variations of the aerodynamic behavior of the components and their respective speed variations.

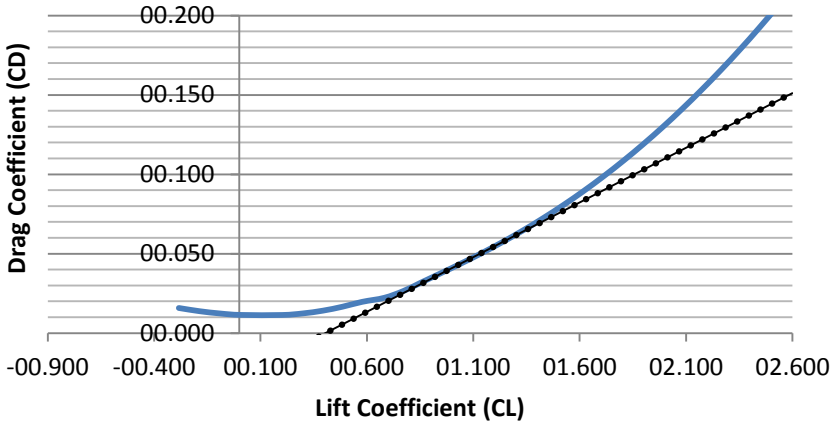

Graph 4.3 – Aircraft Drag Polar

4.4 Flutter Analysis

Due to the wing having a very high aspect ratio, we had to perform a flutter analysis. To do so we utilized a criteria found in the paper *Simplified Flutter Prevention Criteria For Personal Type Aircraft* [5] which states that the torsion flexibility factor, F, given by the Equation 4.2, must be less than $200/V_d^2$.

$$F = \int Q_i C_i^2 \, ds \qquad (4.2)$$

Where Q_i is the wing torsion on the station, *i*, caused by a unit torsional movement applied on the trailing edge of the station; C_i is the chord length of the wing in the station *i* [m]; *ds* is the increment of *b*. The strategy adopted was a less tapered wing with only one type of profile from the root to the tip. According to the formulation exposed above, we obtain $F = 0.32404 < 0.413223$.

4.5 Drag Analysis

According to ANDERSON [7], the accuracy of the performance calculations depends on the quality of the aerodynamic data. The correct estimates of drag provide qualitative data used to make decisions during the aerodynamic design; therefore it is of the utmost importance for the correct evaluation of its actual capacities.

The team has consulted HOERNER [8] who expresses the aerodynamic forces in terms of dynamic pressure, utilizing the concept of drag area which is useful in cases where the reference area is not apparent. Therefore, this was used to estimate the contribution to drag from building and superficial imperfections. In this way it was possible to prevent the influence of each component to and redraw it when the drag was prohibitive, until we obtain a final configuration of most aerodynamic efficiency.

The method of the equivalent length was used in order to determine the C_{D0} of the aircraft lift surfaces. This presupposes that the friction drag contribution of each component is equivalent to a flat plate having the same wetted area and same characteristic length.

In order to estimate the wing C_{D0}, we assume that the fuselage influence over it is small, since the fuselage is located below the wing, presupposing a laminar flow over the fuselage. Therefore, the Equation 4.3 for a flat plate was used:

$$C_f = \frac{1{,}328}{\sqrt{Re_L}} \qquad \textbf{(4.3)}$$

The contribution of the tail-unit to the drag was evaluated by considering the downwash produced by the wing, fuselage and the tail-boom interference over the empennage. We also assumed that the flow is turbulent. For flat plates, Equation 4.4 was utilized for the drag estimation and zero lift in a turbulent flow:

$$C_f = \frac{0{,}074}{Re_L^{0,2}} \qquad \textbf{(4.4)}$$

In order to estimate the fuselage drag we have assumed that the flow is, since the beginning, turbulent due to the propeller slipstream. Therefore the Eckert Equation was utilized since it deals with a blunt body in a completely turbulent flow.

$$C_{f,turb} = \frac{A}{(\log Re)^b (1+cM^2)^d} \qquad \textbf{(4.5)}$$

The proportionality coefficient deduced by Eckert are constants of values A = 0.455, b = 2.58, c = 0.144 and d = 0.58.

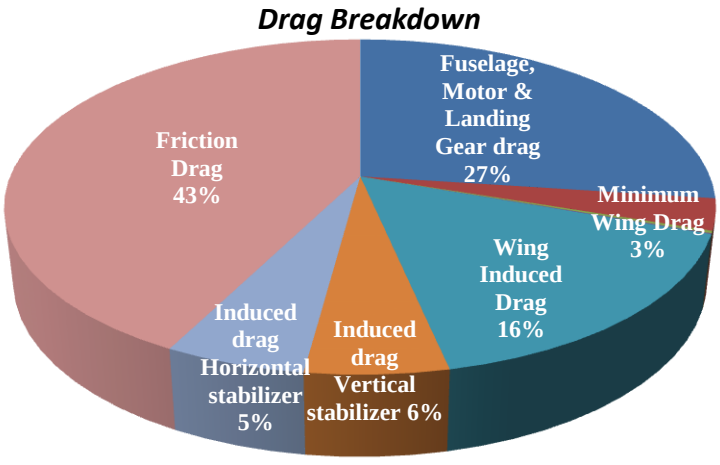

Graph 4.44 – Drag Contributions

5. STABILITY AND CONTROL

An aircraft is stable if after undergoing a disturbance it can return to its original position using the aircraft pitch, roll and yaw commands. The stability analysis is divided into static and dynamic analysis and is further divided into longitudinal, directional and lateral.

5.1 Static Stability

5.1.1 Longitudinal

For the static stability longitudinal analysis, RAYMER [1] affirms that the derivative of the pitch moment in relation to the angle of attack must be negative. The equation that applies to this case is given by:

$$\boldsymbol{Cm_{\alpha} = -C_{L\alpha}(X_{np} - X_{CG})} \qquad \textbf{(5.1)}$$

Where X_{np} is the point in which Cm_{α} = 0 and does not depend on the CG, RAYMER [1] says that the static margin must be positive and over 5%.

Using the *software Tornado*®, the static margin was calculated. In the *software AVL*® we obtained X_{cg} and X_{np}, the subtraction of these two terms is equal to *MS*, therefore the obtained values confirm the values obtained. The data is presented in the Table 5.1.

Table 5.1 – Values for the Longitudinal Stability

X_{np}	X_{cg}	MS	$C_{L\alpha}$ $[rad^{-1}]$
0.1997	-0.0569	0.2567	5.5090

Replacing these values in the Equation 5.1 we get Cm_{α} = -1.4144 [rad^{-1}]. According to CORKE [9], the Cm_{α} value must be negative and assume a value between -1.5 and -0.16. Since the Cm_{α} obtained is situated in this margin, we conclude that the aircraft is longitudinaly stable.

5.1.2 Directional

The static stability directional analysis is given by, according to CORKE [9], the Cn_{β} coefficient.

$$\boldsymbol{Cn_{\beta} = (Cn_{\beta})_{fus} + (Cn_{\beta})_{w} + (Cn_{\beta})_{EV}} \qquad \textbf{(5.2)}$$

The Table 5.2 presents the values obtained for the Cn_{β} calculation:

Table 5.2 – Static directional stability table

Fuselage	$l_{fus} = 0.5196\ [m]$	$AR = 10.5$	$CV_{EV} = 0.035$
	$h_{fus} = 0.1746\ [m]$	$\bar{c} = 0.290\ [m]$	$\alpha_{EV}\eta_{EV} = 1.081$
	$Vol_{fus} = 0.01495\ [m^3]$	$C_L = 2.080\ [rad^{-1}]$	$(C_{L\alpha})_{EV} = 6.283\ [rad^{-1}]$
	$S_w = 0.8600\ [m^2]$	$X_{cg} = 0.03\ [m]$	$(Cn_{\beta})_{EV} = 0.2376\ [rad^{-1}]$
	$(Cn_{\beta})_{fus} = -0.007533\ [rad^{-1}]$	$(Cn_{\beta})_{w} = 0.03342\ [rad^{-1}]$	

According to the same reference, the acceptable values for Cn_β must be contained between 0.08 and 0.28. Using the values showed in the Table 5.2 above we can obtain a value for $Cn_\beta = 0.2634$ [rad^{-1}]. Therefore following this method we conclude that the aircraft is directionally stable.

5.1.3 Lateral

For the lateral stability analysis, we use the $C\mathcal{L}_\beta$ coefficient (Equation 6.3) and this value must be less than zero. However since the terms of the equation are difficult to evaluate, CORKE [9] suggests an approximation, given by the Equation 5.4:

$$C\mathcal{L}_\beta = (C\mathcal{L}_\beta)_W + (C\mathcal{L}_\beta)_{EV} + (C\mathcal{L}_\beta)_{W-F} \qquad (5.3)$$

$$C\mathcal{L}_\beta = -Cn_\beta \qquad (5.4)$$

Following Corke, for the aircraft to be considered laterally stable the following inequality must hold: $-0.9 \leq \frac{C\mathcal{L}_\beta}{C_L} \leq -0.05$. As $C\mathcal{L}_\beta = -0.2634\ [rad^{-1}]$ and $\frac{C\mathcal{L}_\beta}{C_L} = -0.1266\ [rad^{-1}]$. We conclude the aircraft is laterally stable since the values found are less than zero.

5.2 Dynamic Stability

5.2.1 Longitudinal and Lateral

According to the norm JAR-VLA [12], every short period oscillation (not including the latero-directional that occurs between the stall and the maximum speed) must be critically damped using the primary controls.

In order to evaluate the longitudinal dynamic analysis, the motion equations were written in a state-space format. This technique allows the motion variables to be written in transient form, which allows the team to evaluate the whole behavior of the aircraft during its flight envelope. This method makes use of the transfer function, where the input function represents small aircraft disturbances. This allows these equations to be solved by numerical methods. Using the software *MATLAB*®, a complete evaluation could be made. The correspondent matrix equations are show below.

$$\vec{M}\dot{\vec{x}} = \vec{A'} + B'\vec{U}(t) \qquad (5.5)$$

$$M = \begin{bmatrix} m & -\dot{X}_{\dot{w}} & 0 & 0 \\ 0 & (m - \dot{Z}_{\dot{w}}) & 0 & 0 \\ 0 & -\dot{M}_{\dot{w}} & I_y & 0 \\ 0 & 0 & 0 & 1 \end{bmatrix} \quad A' = \begin{bmatrix} \dot{X}_u & \dot{X}_w & (\dot{X}_q - m_{W_e}) & -mgcos\theta_e \\ \dot{Z}_u & \dot{Z}_w & (\dot{Z}_q + m_{U_e}) & -mgsen\theta_e \\ \dot{M}_u & \dot{M}_w & \dot{M}_q & 0 \\ 0 & 0 & 1 & 0 \end{bmatrix} \quad B' = \begin{bmatrix} \dot{X}_\eta & \dot{X}_\tau \\ \dot{Z}_\eta & \dot{Z}_\tau \\ \dot{M}_\eta & \dot{M}_\tau \\ 0 & 0 \end{bmatrix}$$

The aircraft response is calculated taking into account a 1° degree elevator deflection, and its correspondent transfer functions are determined adopting the hypothesis that the motion is

constrained to small disturbances. Observing the Graph 5.2 below, we conclude that this aircraft satisfies the requirements imposed by the norm.

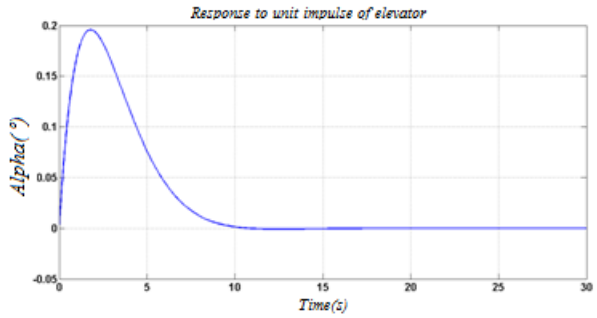

Graph 5.1 – Unit impulse Longitudinal Elevator response

5.2.2 Latero-Directional

NELSON [10] affirms that for a dynamic latero-directional analysis, one must use the motion equations that take into account the lateral force, the roll moment and pitch moment. These can be rearranged in state-space format and then it will become possible to obtain the necessary derivatives. The stability calculations can be obtained by the relation given by the matrix below, where the values were calculated using the *software MATLAB*®.

$$\begin{bmatrix} \frac{Y_\beta}{V_{trim}} & \frac{Y_p}{V_{trim}} & -\left(1-\frac{Y_r}{V_{trim}}\right) & \frac{g\cos\theta_0}{V_{trim}} \\ L_\beta & L_p & L_r & 0 \\ N_\beta & N_p & N_r & 0 \\ 0 & 1 & 0 & 0 \end{bmatrix} = \begin{bmatrix} -5.61 & -0.71 & -1.71 & 0.83 \\ -75.99 & -267.03 & -267.03 & 0 \\ 16.99 & -27.12 & -27.12 & 0 \\ 0 & 1 & 0 & 0 \end{bmatrix} \quad \textbf{(5.6)}$$

Following this method two real roots and two imaginary roots were found, that characterize the response to the spiral, dutch roll and roll modes. The values obtained for the roots are given below (Table 5.3), as the graph obtained (Graph 5.3):

Table 5.3 – Roots obtained

$\boldsymbol{\lambda}$ **(*spriral mode*)**	$-0.0104 \cdot 10^2$
$\boldsymbol{\lambda}$ **(*roll mode*)**	$-2.9431 \cdot 10^2$
$\boldsymbol{\lambda}$ **(*dutch roll mode*)**	$-0.0221(\pm 0.0362i)$

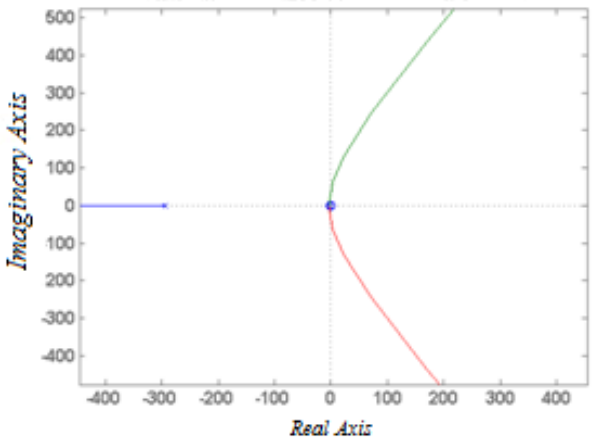

Graph 5.2 – Roots in relation to $C_{n\beta}$

Since the roots obtained are in the left semi-plane, by the classical control theory, we can assure that the aircraft is latero-directional stable.

5.3 Control

The concept of control is employed when one wants to change the fight conditions of the aircraft. This concept is important to the correct sizing of the aircraft servo-mechanisms. It also helps to size the control surfaces that better satisfy the necessities posed by the aircraft. For the control calculation it is necessary to obtain the hinge moment coefficients, obtained by the team using the *software AVL*® and recorded in Table 5.4.

Table 5.4 – Hinge Moment Coefficients

$Ch_{\delta EH}\ [rad^{-1}]$	$Ch_{\delta EV}\ [rad^{-1}]$	$Ch_{\delta aileron}\ [rad^{-1}]$
0.0786	−0.1941	−0.2214

5.3.1 Elevator Analysis

The following Equation 5.7 gives the speed required for a steady level flight.

$$V_{trim} = \sqrt{2 \cdot \frac{W}{\rho S C_{Ltim}}} \qquad (5.7)$$

Considering a particular case in which we want to fly at a speed less than the cruise speed to compensate the dynamic pressure, we must increase the C_{Ltim} on the same proportion. An increase in the C_{Ltim} can be obtained in two ways: either increasing the deflection angle or shifting the aircraft CG location. Since the CG position is related to the cargo-bay geometry, we use the first option for the study of a longitudinal control. According to ANDERSON [2], the elevator deflection angle is given by the Equation 5.8. Its efficiency must be sufficient to produce a moment on the tail in relation to the C.G at the maximum take-off speed.

$$\delta_{trim} = \frac{C_{m0} + (C_{m\alpha}\alpha)}{v_{EH} C_{L\alpha EH}} \qquad (5.8)$$

Where C_{m0} = -0.1385 [rad^{-1}]. In this way, variating the CG position we obtained the Graph Graph 5.3.

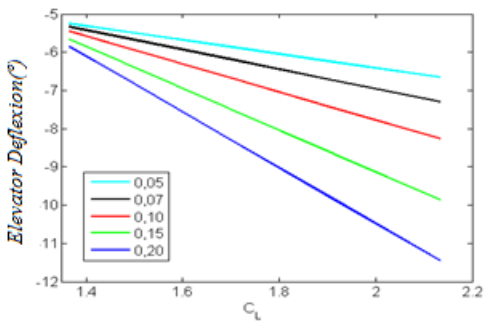

Graph 5.3 - Elevator deflection vs. C_L aircraft

Observing Graph 5.4, we conclude that the elevator deflection satisfies the values demanded during the flight for a variation between 5% to 20% of the static margin and they are capable of changing the profile camber generating in this way a hinge moment. TORENBEEK [11] indicates the Equation 5.9.

Integrating the Equation 5.9 and adopting a reference point ($\delta_{EH} = 0°$ for $V = V_{trim}$), we could obtain the Graphs 5.5.1 and 5.5.2.

$$\frac{\partial \delta_{EH}}{\partial V} = \frac{2C_L(X_{np} - X_{CG})S\bar{c}}{C_{LEH}VS_{EH}X_{EH}} \qquad \textbf{(5.9)}$$

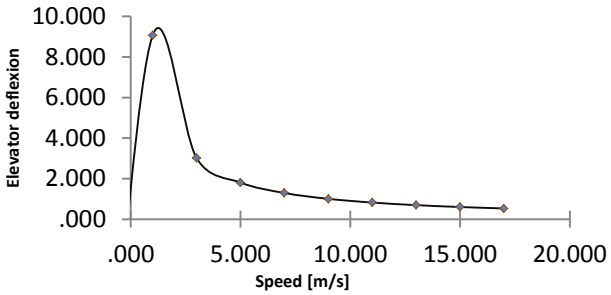

Graph 5.5.1 – Speed vs. Elevator Deflection

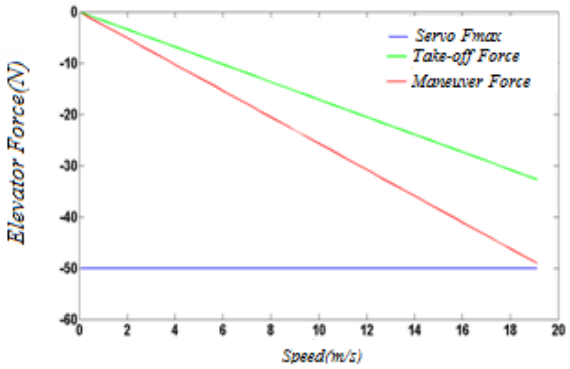

Graph 5.5.2 – Force on elevator vs. Speed

We could analyze the force demanded by the elevator utilizing the moment equation as showed in the Graph 5.5.2, and size the servo for the elevator.

5.4 Latero-directional Control

5.4.1 Rudder Analysis

RAYMER [1] characterizes an "efficient" rudder as one that has a chord length in relation to the vertical stabilizer between 25% and 50%. In the beginning the team has used the minimum value of 25%.

For the evaluation of the forces generated by the rudder, Equation 5.10 given by ROSKAN [6] was utilized:

$$\frac{\partial F_{EV}}{\partial \beta} = \frac{G_{EV}\eta_v q S_{EV}\bar{c}_{EV}Ch_{\delta EV}Cn_{\beta free}}{Cn_{\delta EV}} \qquad \textbf{(5.10)}$$

Using the *software AVL*®, we got $Cn_{\beta free} = 0.0995$ and $Cn_{\delta EV} = -0.0153$. Integrating the Equation 5.10 and knowing a point of this curve (the point where $F_{EV} = 0$ [N] for $Cn_{\delta EV} = 0°$) we obtained the following Graph 5.6.

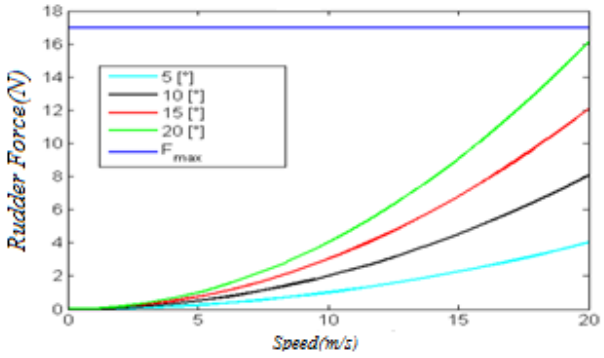

Graph 5.6 – Force on rudder vs. Speed

By observing the Graph 5.6, we conclude that the force in the rudder is 17 [N].

5.4.2 Aileron Design and Analysis

Equation 5.11 given by ROSKAN [6] was utilized to evaluate the ailerons:

$$F_{al} = qS_{al}\overline{c_{al}}G_{al}(-2Ch_{\delta al}\delta_{al}) + G_{al}K_{EV-al}\delta_{EV} \qquad (5.11)$$

Then, the following graphs were obtained:

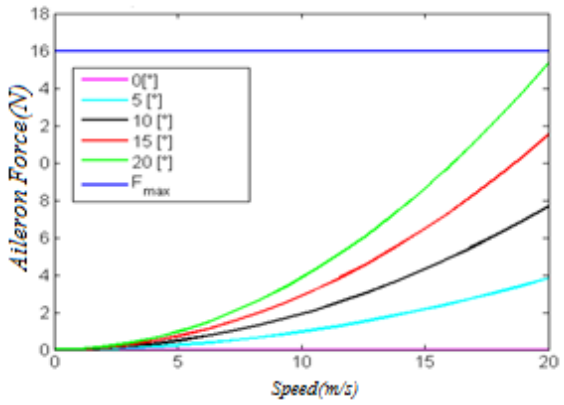

Graph 5.7 – Force on aileron vs. Speed(Rudder at 0°)

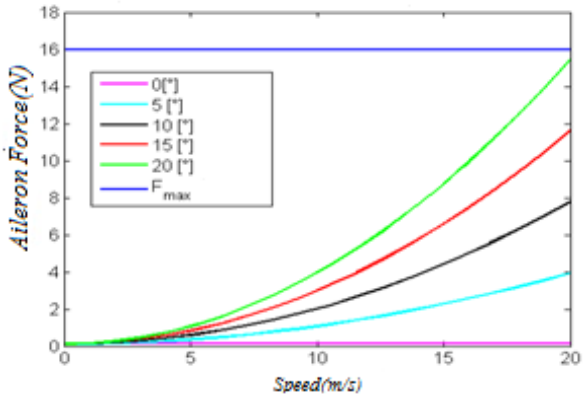

Graph 5.8 –Force on aileron vs. Speed (rudder at 20°)

6. PERFORMANCE

6.1 Power Plant Selection

The selection of the power plant has great importance in the development of the aircraft design because the power plant has a crucial role in the mission that the aircraft was designed to accomplished.

The engines that were traditionally used by the competition are presented, with some of its characteristics in the Table 6.1.

Table 6.1– Engine Characteristics

Engine	RPM	Power [HP]	Mass [g]
O.S.® 0.55AX	2000 – 17000	1.75	404
Magnum XLS® - 61	2000 – 16000	1.90	638

The Table 6.2 is composed by the data gathered in Brazil for the following propellers: *JZ*® 13x4, *APC*® 13x4, *JXF*® 13x6 and *MAS*® 13x6. The Graph 6.1 shows the available thrust for each propeller tested varying the speed.

Table 6.2- Power Plant Static test

Propeller	13x6 JXF	13x6 MAS	11x6 JZ	11x7 APC
Rotations [RPM]	9210	8610	10690	12090
Mass[g]	28.7	25	26.8	50.7
Measured Thrust	26 [N]	25 [N]	30 [N]	32 [N]

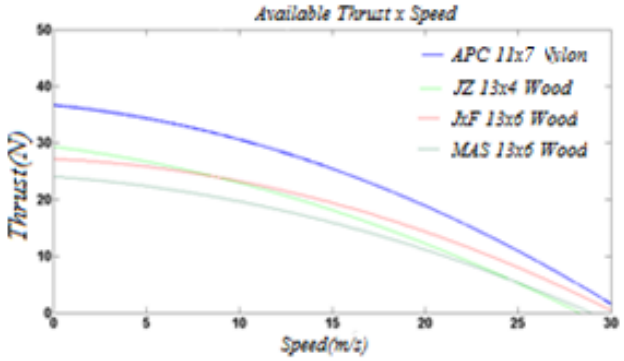

Graph 6.1– Available Thrust vs. Speed

The higher the available thrust of the power plant during the take-off, the higher the payload that can be carried by the aircraft. Understanding this in addition to the experience gained in Brazil, we concluded that the propeller that better suits the project is *APC®* 11x7 Nylon sport version.

Having acquired the available and required thrust, we are able to experimentally determine the power at each thrust level. The power curves obtained could be visualized in Graph 6.2. The Graph 6.3 illustrates the relation between thrust and aircraft drag.

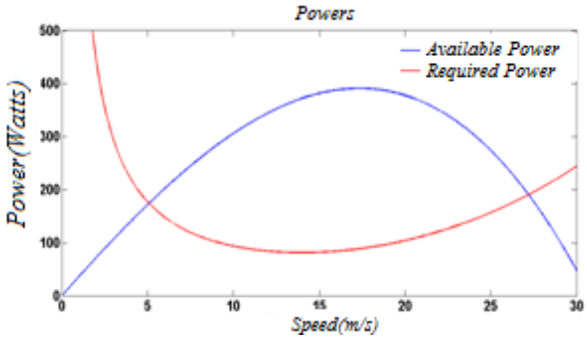

Graph 6.2 – Available Thrust and Required Thrust

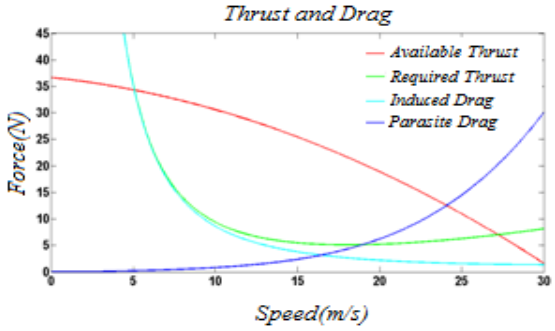

Graph 6.3 – Aircraft Thrusts and Drags

6.2 Take-off

The take-off analysis was based on the method by KRENKEL[18], the numerical adaptations proposed by LYNN [19] and computationally implemented in the *software MATLAB®*.

The original method by KRENKEL [18] approaches the take-off and climbing phases, but do not take into account the instant that the aircraft rolls. Therefore for higher accuracy in the data obtained, the take-off phase *was included in the calculations according to the methodology proposed by* NICOLAI [20]. The code input data was set for: total take-off distance 50 [m] and the obstacle height in the end of the runway 10 [cm], also the values for C_{Lg} and C_{Dg} were adjusted to ground effect influence based in a study proposed by ROSKAN [6].

In order to evaluate the take-off length required in relation to the payload, a method very similar to the method utilized to calculate the maximum cargo was used, constraining this time the runway length each iteration. Through these means, the relation illustrated in the Graph 6.4 surfaces. The analyses realized were based in the calculations for the following altitude values 0 [m], 400 [m], 800 [m] and 1100 [m].

Table 6.3- Take-off data summary

Carried Payload= 10,000 [kg]

Take-off Speed	13.42	$[m/s]$
Obstacle Height	9.98	$[cm]$
Take-off Total Distance	47.50	$[m]$
Climb Angle	4.61	[°]
Rate of Climb	1.75	$[m/s]$
Take-off Time	6.87	$[s]$

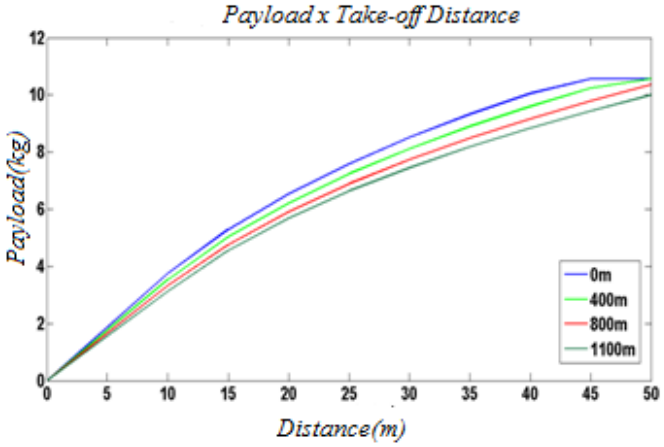

Graph 6.4– Payload vs. Take-off distance varying altitude

The data in the Table 6.3 summarizes the main take-off parameters for an altitude-density of 1100 [m]. Lastly, it was assumed that the aircraft achieves take-off after the obstacle height, then it's made possible to validate the procedure.

6.3 Flight Performance

In order to evaluate the flight performance studies were carried out based on the proposals by ANDERSON [7] and ROSKAN [6]. The main speeds are presented in the Table 6.4.

Table 6.4 – Characteristic Speed for 0 [m] and 1100 [m]

	0 [m]	**1100 [m]**
Stall Speed	10.54 [m/s]	10.86 [m/s]
Maximum Speed	20.56 [m/s]	21.18 [m/s]
Maximum autonomy speed	17.96 [m/s]	18.51 [m/s]
Dive Speed	30.58 [m/s]	30.50 [m/s]

6.4 Climb and Glide Performance

For the climb performance we used an equation that relates the remaining power to your total weight in order to find the rate of climb according to the Equation 6.1. The Graph 6.5 illustrates the climb rate for the altitudes of 0 [m] and 1100 [m]; this confirms the altitude influence in the result.

Table 6.5 – Rate of Climb

Parameters	**0 [m]**	**1100 [m]**
Maximum Angle of climb	11.03 [°]	9.94 [°]
Speed for Maximum Angle	11.22 [m/s]	11.33 [m/s]
Maximum Rate of Climb	2.68 [m/s]	2.42 [m/s]
Maximum Speed Ratio	16.26 [m/s]	16.19 [m/s]

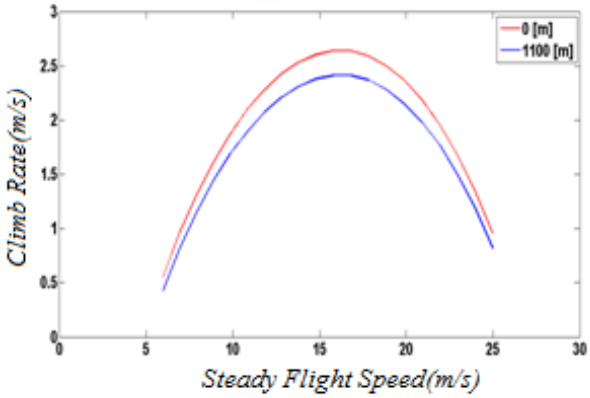

Graph 6.5 – Climb Rate

The rate of climb is analyzed for a power cut-off utilizing the Equation 6.2. The Graph 6.6 illustrates the relation between the vertical descend speed and horizontal speed.

Table 6.6 – Descent Rate

Minimum descend angle	2.39 [°]
Minimum angle speed	17.87 [m/s]
Minimum descend	

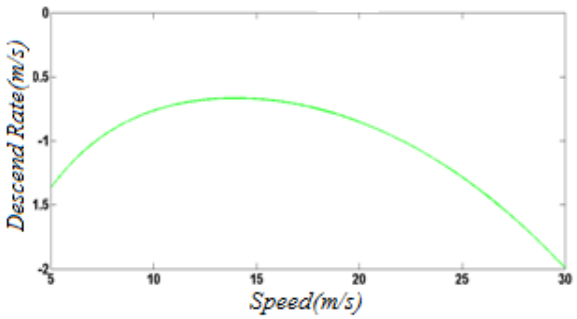

Graph 6.6- Descent Rate

$$R/C = \frac{P_D - P_R}{W} \quad \textbf{(6.1)}$$

$$\boldsymbol{R/D = \sqrt{\frac{2W}{\rho S(C_L^3/C_D^2)}}} \quad \textbf{(6.2)}$$

6.5 Turning Performance

The study of the turning performance was made according to the methodology proposed by ANDERSON [7] (Equation 6.3 and 6.4). The minimum turning radius was found for a maximum cargo to be 8.48 [m] and an angle for minimum radius of 76.34°. The Graph 6.7 illustrates the total aircraft weight versus turning radius. The Graph 6.8 shows the minimum angle for a minimum turning radius.

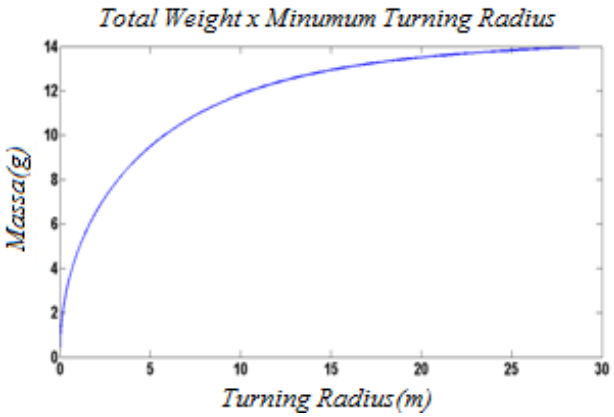

Graph 6.7- Total Weight vs. Minimum Turning Radius

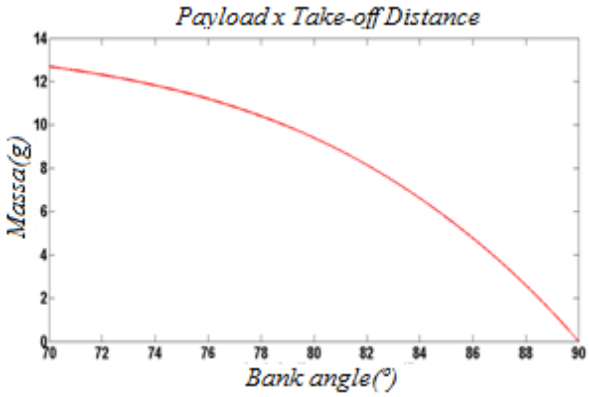

Graph 6.8 – Total mass vs. turning angle

$$\boldsymbol{r = \frac{4K(W/S)}{g\rho(T/W)\sqrt{1-4KC_{D0}/(T/W)^2}}} \quad \textbf{(6.3)}$$

$$\gamma = \tan^{-1}\left(\frac{V_{máxL/D}^{\,2}}{gr}\right) \quad \textbf{(6.4)}$$

6.6 Flight Level

In order to calculate the flight level, a routine was implemented in order to obtain an envelopment that is capable to estimate the minimum speed, maximum speed and flight level. In this study the load factor is considered to be $\eta_{max} = 3.8$.

6.7 Landing

In the landing study, the team implemented a routine through the *software MATLAB®*, using the landing distances developed by RODRIGUES [21] as the basis. The Table 6.7 illustrates the values obtained by this analysis.

Table 6.7 – Landing Characteristics

	0 [m]	**1100 [m]**
Landing distance(no brakes are employed)	145.65 [m]	154.63 [m]
V_{td}	12.12 [m/s]	12.49 [m/s]

Table 6.8 - Ideal friction coefficients

50 meters	0.26
75 meters	0.16

6.8 Mission Time

In order to obtain the mission time, every flight phase had its duration calculated (Table 6.10), utilizing the techniques proposed by RODRIGUES [20] and ANDERSON [7], we obtained a total sum of 97.40 [s].

Table 6.9 – Flight Time

Take-off	6.87 $[s]$
Climb	17.12 $[s]$
Turn	26.45 $[s]$
Descent	40.54 $[s]$

Table 6.10 – Average Fuel Consumption

Consumed Volume	50 $[ml]$
Consumption Time	233.47 $[s]$
Average Consumption	0.21 $[ml/s]$
Total Flight Time (180 cc)	636.93 $[s]$

Knowing the total mission time and the average consumption it was possible to select the fuel tank that better fits the project. Table 6.10 shows the fuel consumption of the power plant at maximum power. Therefore, the fuel tank selected was a *DUBRO® S-8.*

7. LOADS AND STRUCTURE

7.1 Structural Design

During the preliminary analysis, the norm JAR-VLA [12] was extensively used, especially in the estimation of aerodynamic loads and ground loads. In this way, the critical load for each flight scenario was determined. During the detailed design phase the software *Tornado* in *MATLAB®* was used to provide the load distribution which in turn was used to size the components.

The *softwares Microsoft Excel®, Ansys ® and CATIA®* were used to design the components. In this phase, special care was taken to use failure criterion that better suit the component under study. For the structural design the following references were used BARROS [3] and ISCOLD [13].

7.2 Flight Envelope (V-n)

The V-n diagram was built considering a maximum load factor of $\eta_{max} = 3.8$ and a minimum load factor of $\eta_{min} = -1.5$ for the maneuver envelope, according to JAR-VLA [12] paragraph JAR-337.

The values for minimum, average and maximum speed were used to find the gust values for U_c and U_d, these being respectively $U_c = 2.612$ [m/s] the maximum average speed and $U_d = 1.121$ [m/s] the minimum average speed. The results are show below:

Table 7.1 - V-n Diagram Parameters

Flight Envelope	
Maneuver	**Gust**
V_c = 24.39 [m/s]	U_c = 2.612 [m/s]
V_A = 20.33 [m/s]	U_d = 1.121 [m/s]
V_d = 30.49 [m/s]	**Load Factor**

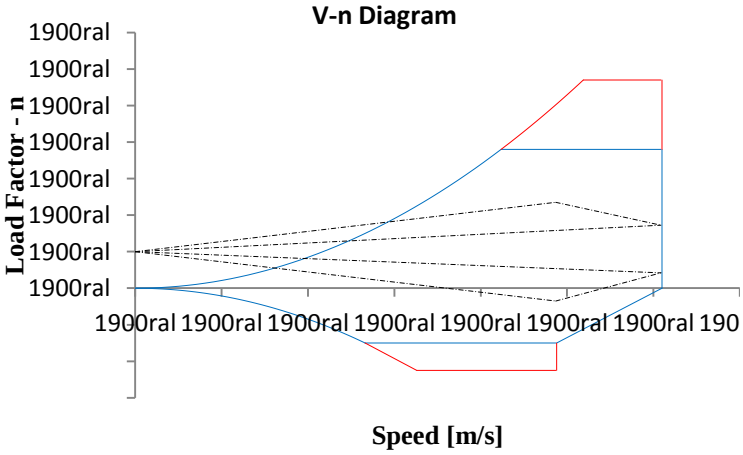

Graph 7.1 - V-n Diagram

7.3 Materials properties

The materials properties were obtained from MATBASE [14] and FOREST PRODUCTS LABORATORY [15].

7.4 Wing Load Determination

The acting stresses were calculated initially with the knowledge of the lifting distribution using the Shrenk method for each flight condition and type of maneuver specified by [12]. The torsion loads were found according to the paragraph JAR-349 and JAR-455. A more depth analysis was performed in the *software Tornado®* for a 20° elevator deflection at cruise speed. The load factor reached, under these conditions, is $\eta_{max} = 3.8$. For a critical load on the wing, the results obtained are shown in the Graphs 7.2 and 7.3.

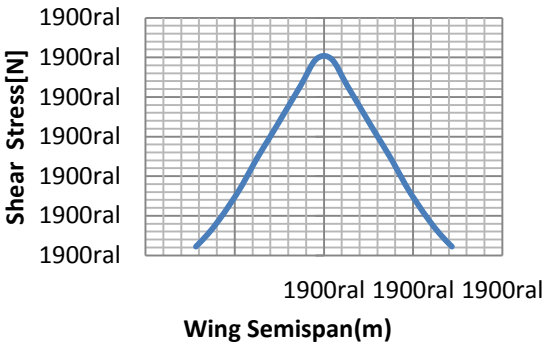

Graph 7.2 – Shear Stress Diagram

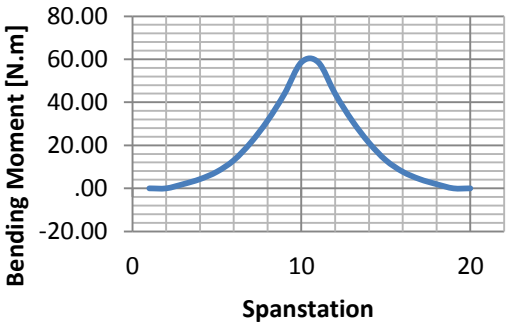

Graph 7.3 – Bending Moment Diagram

The center of shear was defined to be 27%; this corresponds to the thickest section of the profile where the pressure center does not change significantly for high angles of attack. Thus, the torsional stress over the spar is reduced significantly.

Several cross section parameters were studied; the polar moment of inertia and the area were the main parameters and the *Microsoft Excel® Solver* was used. The constraints were set to be the geometrical limitations imposed by the wing profile, in such a manner to minimize the acting stress in order to respect the total safety coefficient of 1.725, obtained by $(FS)x(FQ)$, with respective values of 1.5 and 1.15.. The final configuration is a rectangular beam made of balsa wood—the geometry that presented the highest $(J/S)_{lg}$ ratio.

Aero-elasticity effects were considered due to the high aspect ratio of the wing, the failure criteria was defined as follows: the wing tip cannot exceed 2°; this value was chosen in order to avoid an aileron stall. In the test shown in Figure 7.2, the angle calculated was about 0.73°, considering the situation of a take-off roll, generating a maximum force on the ailerons equal to 16.0 [N], as calculated in the Stability and Control analysis.

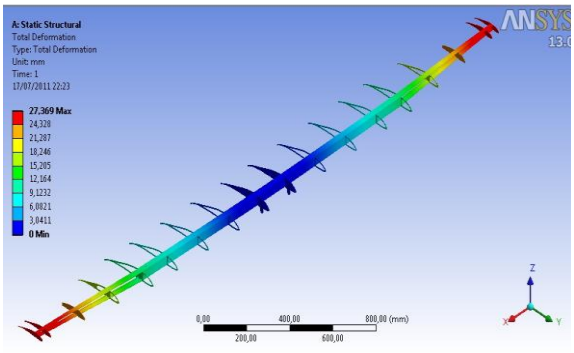

Figure 7.1 – Bending Analysis

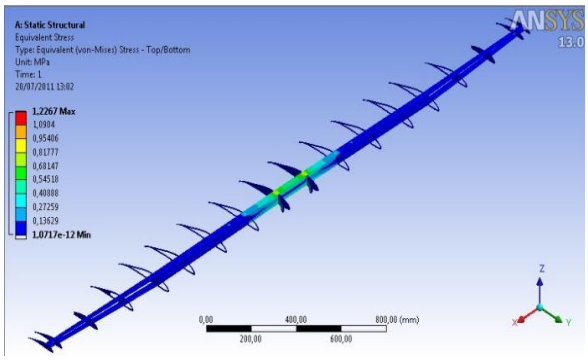

Figure 7.2 – Torsion Analysis

7.5 Front Wheel

The aluminum alloy AA 6061-T3 was chosen. On the drawing in annex number 2, one can find the front wheel drawing. Its 60° rotation movement is possible due to low friction between the UHMW components.

7.6 Landing Gear

The landing gear design was aimed to provide the minimum weight possible and maximum performance to the situation indicated by the JAR-VLA [12]. The configuration was obtained considering mainly the CG location and load distribution between the main wheels and nose. According to RAYMER [1] the turnover angle was obtained and the distance between wheels was calculated.

According to the JAR-VLA [12], the ground factor was set to $\eta_g = 2.67$, calculating a maximum admissible reaction force $R_{max} = 325.3$ [N], given by the Equation 7.1.

$$n_g = \frac{R_{max}}{W} \qquad (7.1)$$

The maximum speed that the structure can resist without touching the ground was calculated considering that at the maximum deflection point there is no kinetic energy, only potential energy. Equating the initial energy to the energy stored due to the deflection, one can obtain the Equation 7.2.

$$\frac{1}{2g} V_{dc}^{\,2} = \left(n_{rd} \cdot n_g \cdot \Delta_{rd}\right) + \left(n_{tp} \cdot n_g \cdot \Delta_{tp}\right) + \Delta_{rd}(k_L - 1) + \Delta_{tp} \cdot (k_L - 1) \qquad (7.2)$$

Considering that the wheels do not undergo deflection, one can adopt Δ_{rd} as zero. Therefore, the maximum descent speed is *0.72* [m/s].

In order to reduce the bending without increasing the component weight and increase the section inertia moment of the cross section, an initial model was designed in CAD and its stress distribution was found using the FEM code embodied in CATIA, and the design was optimized. It was possible to achieve a weight reduction of 42 g. without changing its maximum deflection of 2%.

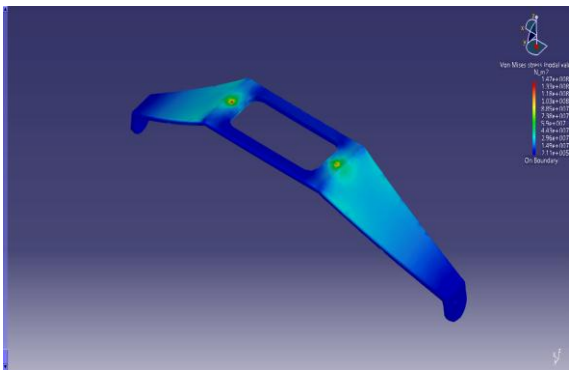

Figure 7.5 – Landing Gear I

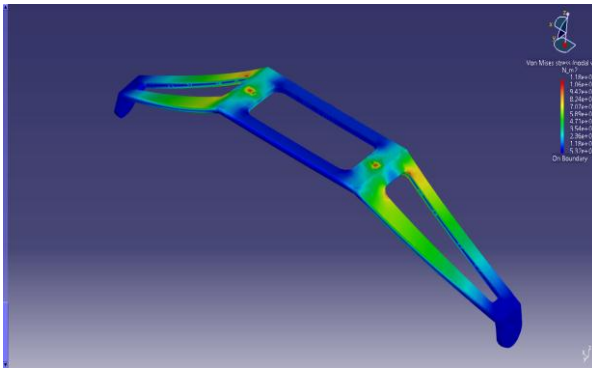

Figure 7.6 – Landing Gear II

Several types of landing were considered to validate the aircraft to all possible landing configurations.

7.7 Level Landing

In order to calculate the energy absorbed at the moment that the front and main landing gear touch the ground, we apply the Equation 7.3. Since both gears touch the ground at the same time in this type of landing, it is important to present the total energy as the energy they must absorb.

$$E_{tp} + E_b = \frac{W \cdot V_{dc}^2}{2 \cdot g} \qquad (7.3)$$

By mean of the above calculation, one obtains *3.25* [J] as the total energy absorbed and by the JAR-VLA 479 calculation, E_{tp} represents 75% and E_b 25% of this value. Comparing E_{tp} = *2.03* [J], generated by the descend ratio calculated in the previous sections with E_{tp} = *2.44* [J], from the Equation 7.3, validated the landing gear sizing.

7.8 Landing on two main gears

The angular acceleration during a pitch maneuver generates an apparent weight on the centroid, which can be evaluated by the Equation 7.4

$$W' = \frac{W}{1 + \frac{Icg^2}{k_y^2} + \frac{c_{at} \cdot h_{CG} \cdot I_{CG}}{k_y^2}} \qquad (7.4)$$

7.9 Wing

Each wing semispan was divided into sections in order to calculate the load distribution according to the methodology presented by BARROS [3], the results are summarized below.

Two tests were realized, one with negative bending and the other with positive bending, representing a landing situation and an in-flight situation respectively.

Table 7.2 - Percentage of applied load in each sector in relation to the total load applied on the wing semispan

Sector	1°	2°	3°	4°	5°	6°	7°	8°	9°
Percentual (%)	18	16.5	15.5	14.5	13	10	7	3.5	2

Table 7.3 – Bending recorded after the load in each wing semispan

Load	$\mathbf{60,9}\ [\boldsymbol{N}]$ (1)	$\mathbf{91,4}\ [\boldsymbol{N}]$ (2)
Negative bending	$26\ [mm]$	$42\ [mm]$
Positive bending	$25\ [mm]$	$34\ [mm]$

(1) BARROS [3] (120 s) / (2) JAR-VLA [12] (30 s)

Analyzing the Table 7.3 and comparing it with the computational tests, we conclude that under critical flight conditions, the spar will resist the acting loads.

7.10 Landing Gear [Model]

According to ISCOLD [13] and the norms JAR-VLA 723-725 [12], we were able to determine the bending caused by the calculated ultimate load. To do so, static tests were made on the landing gear by applying loadings until the limit, 121.8 [N]. The obtained maximum strain was about 2.5 [m].

7.11 Wheels

The team observed that wheels made in nylon UHMW present high shock resistance, low weight and a friction coefficient that suits the project requirements. For mass reduction only one bearing was used in each wheel and relief holes were made.

7.12 Aircraft Empty Weight Estimation

The team placed utmost importance on the weight estimation since this has a major impact on the performance characteristics and maximum payload to be carried. In order to preview the empty weight, the team has determined the density of all the materials employed. These values were inserted in the software *CATIA*®, some optimization was carried out in an overall aspect of the aircraft in order to reduce its gross empty weight.

8. Electrical and Electronics Design

8.1 General Considerations

Analyzing past designs we could conclude that several components were oversized adding extra mass which is undesirable for the project conclusively. This year, we aimed at a maximum weight reduction component by component without interfering with the aircraft controls.

8.2 Radio, Receiver and Servo Selection

The team is using an *AR115 six Channel DSMX Microlite Spektrum*® receiver. The receiver is placed on the tail in order to positively affect CG location.

The aileron and the rudder are actuated by the servos *Hobbico*® CS-35MG and *Hobbico*® CS-12MG respectively, which present more than adequate amounts of torque and metal gears that are highly resistant to shock yielding safer flight of the aircraft. For the engine the servo *HXT-900* was

used. For the front gear the team has opted for the servo *Hobbico*® CS-35MG. The elevator uses a servo *Hobbico*® CS-64MG.

Table 8.1 – Servo Utilized Characteristics

Servo	Qtd.	Component	Voltage [V]	Labeled Torque [kg.cm]	Real Torque [kg.cm]	Mass [g]
HXT-900	1	Motor	4.8	1.6	1.5	9.0
CS-64	1	Elevator	4.8	5.0	4.9	50.0
CS-12MG	1	Rudder	4.8	2.6	2.5	19.0
CS-35MG	3	Aileron and Steering Wheel	4.8	3.2	3.0	28.0
Total	6	---	---	---	---	162.0

8.3 Electric Wire and Power Demand

The highest current consumed by a servo in the circuit is 1.51 [A]. Establishing 24.5% of safety margin in the maximum current supported, we calculated, according to the pattern AWG, a new size for the wiring harness cables: 24 gauge [AWG] which support a maximum current of 2 [A].

The Figure 8.2 shows a plot of current in function of time in the servo CS-64 e CS-12, where the vertical axis represents the current in ampere and the horizontal axis stands for time.

Figure 8.1 – Electrical Current in function of time in the servos CS-64 and NES-331

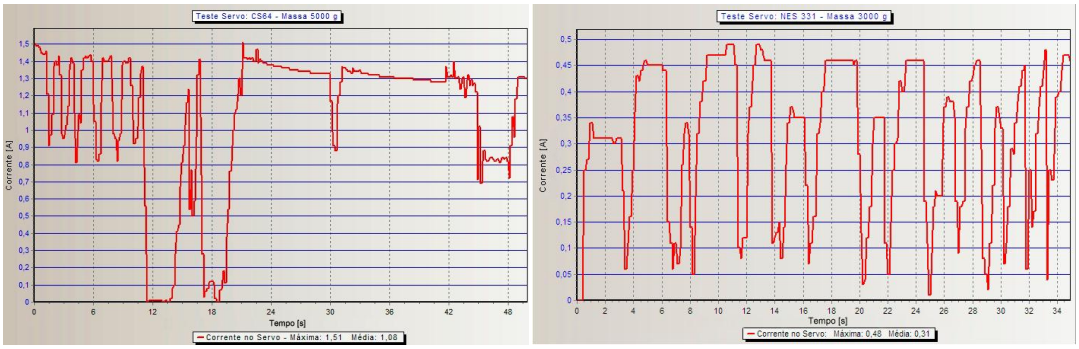

8.4 Battery and Demand Charge

The battery utilized is *SMC Lightning Volts*® SUM1650ML composed of *Li-Po*. Its characteristics are shown in the Table 8.4. Its mass/power ratio is excellent and its recharge time when compared to other batteries is mediocre.

Considering a one minute time interval for the take-off and landing, and about 7 minutes for the flight loft, we obtained the Table 8.5.

Table 8.4 – Battery specifications

Battery	Li-Po
Charge	1650 $[mAh]$
Number of cells	2
Nominal Voltage	7.4 $[V]$
Maximum discharge current	8000 $[mA]$
Mass	84.5 $[g]$

Table 8.5 – Current demand

Component	Quantity	Consumed Load [mAh]
CS-12MG	1	78.49
CS-35MG	3	255.47
CS-64MG	1	153.81
HXT-900	1	51.27
Receiver	1	1.87
Total		540.91

According to BOYLESTAD [17], and considering a 20% safety margin on the load caused by the electrical components, we obtain a load consume of approximately $650\ [mAh]$. The battery utilized provides$1650\ [mAh]$, sufficient load to supply the necessities of this project.

8.5 Voltwatch and Voltage Regulator

The voltwatch selected is a Li-Po battery measurer; it is placed on the aircraft tail, to be located closely to the receiver and the battery. In order to reduce the voltage from 7.4 [V] to approximately 5.0 [V], a *FlightPower*® FT8AVR voltage regulator is utilized according to the Table 8.6, connected in series with the battery.

Table 8.6 –Voltage regulator specifications

Input Voltage	$6.0\ [V]\ to\ 8.4\ [V]$
Output Voltage	$5.0\ [V]\ to\ 6.0\ [V]$
Current	$0\ to\ 5.0\ [A]$
Mass	$53[g]$

8.6 Electrical Diagram

The Figure 8.4 shows the basic electrical schematic and the connection of the servos, battery, voltwatch, switch and the voltage regulator into the receiver.

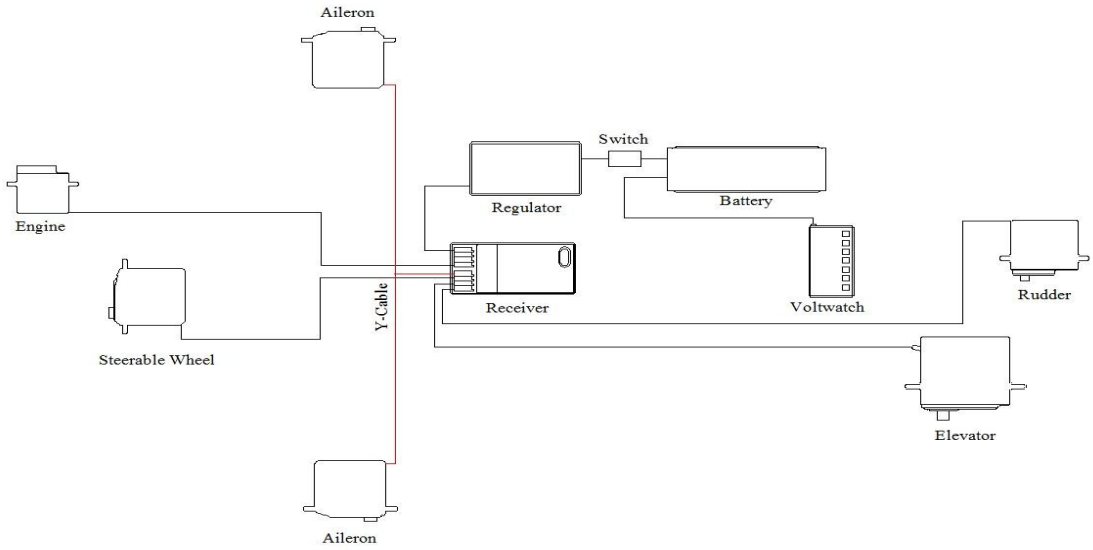

Figure 8.2 – Electrical Diagram

REFERENCES

[1] ABBOTT, I.; VON DOENHOFF, A. *Theory of Wing Sections*. New York: McGraw-Hill, 1949.

[2] ANDERSON JUNIOR, J. *Aircraft performance and design*. New York: McGraw-Hill, 1999.

[3] ANDERSON JUNIOR, J. *Introduction to flight*. New York: McGraw-Hill, 2005.

[4] CORKE, T. *Design of aircraft*. Upper Saddle River: Prentice Hall, 2002.

[5] FONSECA, A. *Curso de mecânica.* 3. ed. Rio de Janeiro: Livro Técnico, 1972. 4v.

[6] HAGE, R.; PERKINS, C. *Airplane performance stability and control.* New York: John Willey and Sons, 1949.

[7] ISCOLD, P. *Introdução às cargas nas aeronaves.* Material didático instrucional do Centro de Estudos Aeronáuticos. Universidade Federal de Minas Gerais, Belo Horizonte, 2002.

[8] JOINT AVIATION AUTHORITIES COMMITTEE. *Joint Aviation Aircraft***:** very light aeroplanes. Netherlands: JAA, 1990.

[9] KRENKEL, A.; SALZMAN, A., *Takeoff Performance of Jet-Propelled Conventional and Vectored-Thrust STOL Aircraft*, Journal of Aircraft, v. 5, n. 5, 1968.

[10] LAU, F.; OLIVEIRA, J. Licenciatura em Engenharia Aeroespacial: semestre de primavera 2004/2005. Disponível em: <http://www.dem.ist.utl.pt/~m_ev/#infor>. Acesso em: 10 jul. 2009.

[11] MATBASE: a leap forward in material data. Disponível em: <http://www.matbase.com/>. Acesso em: 20 jul. 2009.

[12] MEGSON, T. *Aircraft structures for engineering students*. 3. ed. Amsterdan: Elsevier, 1999.

[13] RAYMER, D. *Aircraft Design***:** a conceptual approach. Washington: AIAA Education Series, 1992.

[14] ROSA, E. *Introdução ao projeto aeronáutico*: uma contribuição à competição SAE AeroDesign. Colaboração de Juliano Toporoski. Florianópolis, USFC/GRANTE: Tribo da Ilha, 2006.

[15] ROSKAN, J. *Airplane Design*: part IV – preliminary calculation of aerodynamic, thrust and power characteristics. Lawrence, University of Kansas: AIAA Education Series, 1990.

[16] SCHLICHTING, H.; TRUCKENBRODT, E.; RAMM, H. *Aerodynamics of the Airplane.* New York: Graw-Hill, 1979.

[17] TORENBEEK, E. *Synthesis of subsonic airplane design*. 2 ed. Rotterrdan: Nijgh-Wolters-Noordhoff, 1976.

APPENDIX A

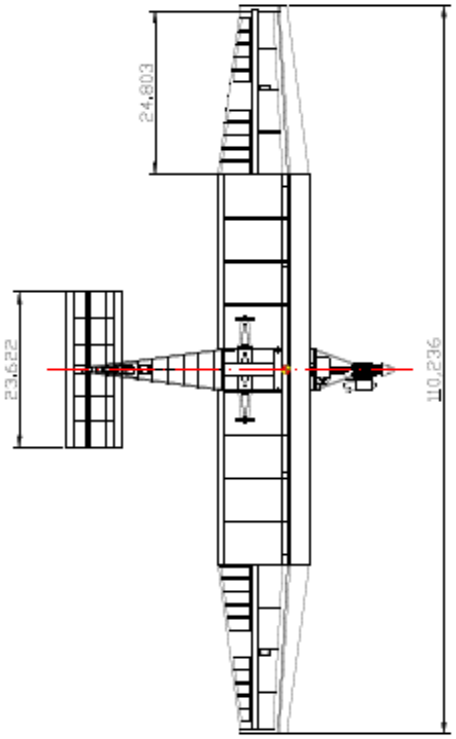

Top View

C.G Location

The Flying Spear		
Main Dimensions (in)		
L	Length	51,338
H	Height	18,071
B1	Wingspan	110,236
B2	Elevator span	23,622
Total		203.267
General Characteristics		
Wing		
Wing Area (in²)		1302,003
Aspect Ratio		10,5
Profile		Uiriâ1540
Horizontal Emp.(EH)		
Area (in²)		204,600
Aspect Ratio		3,3
Profile		NACA-0016
Volume Coef.		0,25
Vertical Emp. (EV)		
Area (in²)		62,001
Aspect Ratio		1,6
Profile		NACA-0016
Volume Coef.		0,035
Empty Weight		3,000 kg

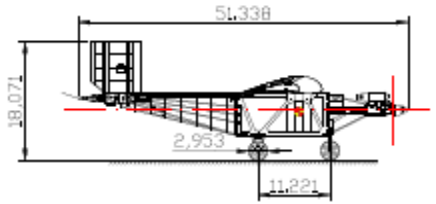

Right Side View

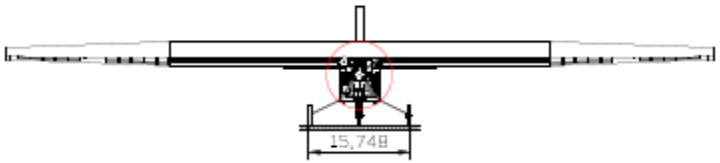

Front View

THE FLYING SPEAR TEAM - 039			
Florida State University FAMU-FSU College of Engineering			
SAE Aero Design® East - 2012			
Autors:	**Design:** The Flying Spear Team		
Three Views		**Sheet Plant n°:**	1/2
		Scale:	1:18
Date:	03/07/2012	**Unity:**	in

APPENDIX B

Florida State University: The Flying Spear – Tallahassee, FL

Payload Graph

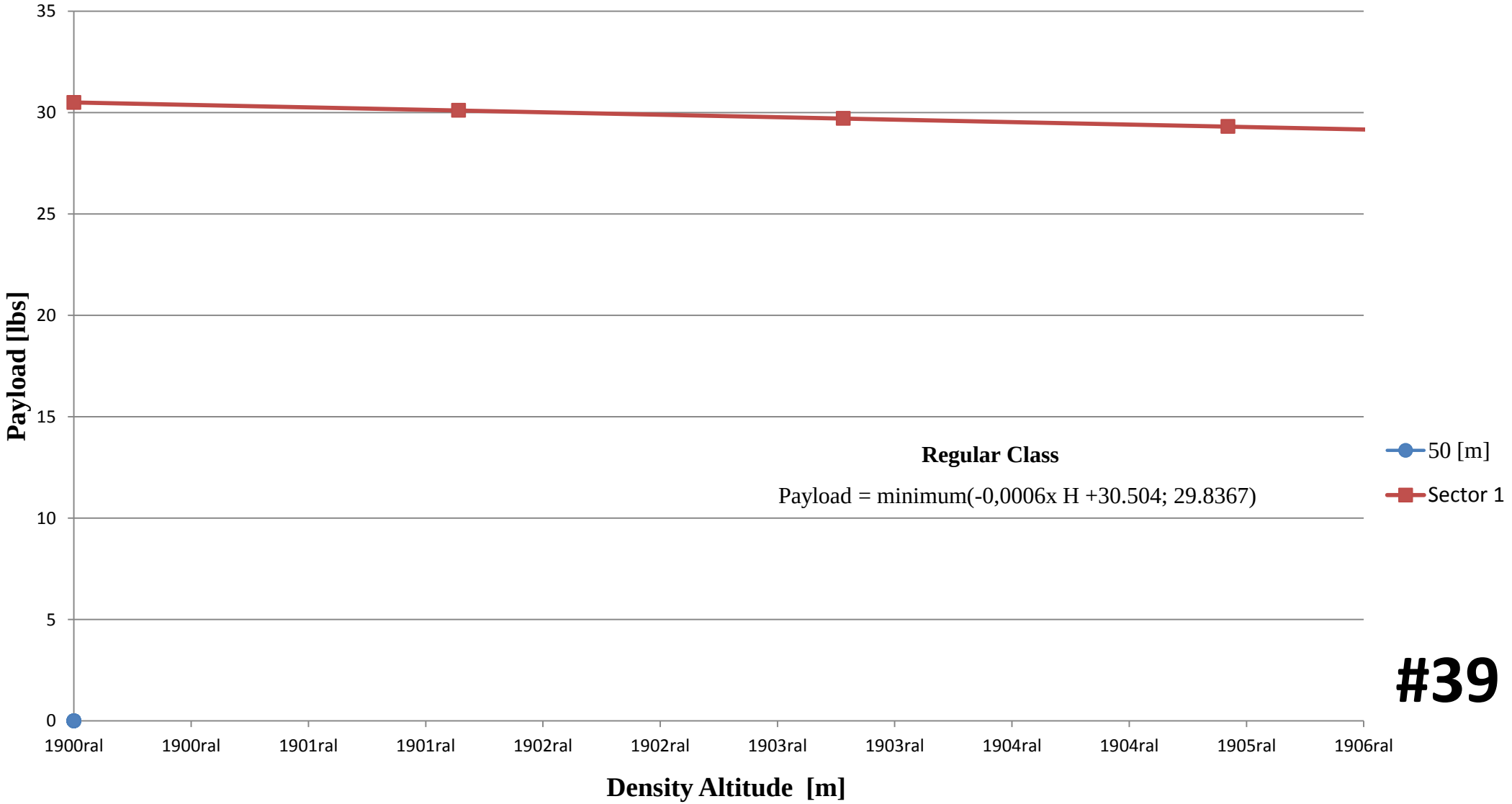

#39